JOURNAL OF GEOPHYSICAL RESEARCH, VOL. 104, NO. D20, PAGES 24,509–24,525, OCTOBER 27, 1999

The climate of the Last Glacial Maximum: Results from a coupled atmosphere-ocean general circulation model

Andrew B. G. Bush

Department of Earth and Atmospheric Sciences, University of Alberta, Edmonton, Canada

S. George H. Philander

Program in Atmospheric and Oceanic Sciences, Department of Geosciences, Princeton University
Princeton, New Jersey

Abstract. Results from a coupled atmosphere-ocean general circulation model simulation of the Last Glacial Maximum reveal annual mean continental cooling between 4° and 7°C over tropical landmasses, up to 26° of cooling over the Laurentide ice sheet, and a global mean temperature depression of 4.3°C. The simulation incorporates glacial ice sheets, glacial land surface, reduced sea level, 21 ka orbital parameters, and decreased atmospheric CO_2. Glacial winds, in addition to exhibiting anticyclonic circulations over the ice sheets themselves, show a strong cyclonic circulation over the northwest Atlantic basin, enhanced easterly flow over the tropical Pacific, and enhanced westerly flow over the Indian Ocean. Changes in equatorial winds are congruous with a westward shift in tropical convection, which leaves the western Pacific much drier than today but the Indonesian archipelago much wetter. Global mean specific humidity in the glacial climate is 10% less than today. Stronger Pacific easterlies increase the tilt of the tropical thermocline, increase the speed of the Equatorial Undercurrent, and increase the westward extent of the cold tongue, thereby depressing glacial sea surface temperatures in the western tropical Pacific by ~5°–6°C.

1. Introduction

One of the more perplexing problems confronting scientists attempting to reconstruct the climate of the Last Glacial Maximum (LGM) is the mounting evidence for tropical cooling of ~6°C [*Guilderson et al*., 1994; *Stute et al*., 1995; *Rind and Peteet*, 1985; *Thompson et al*., 1995]. This cooling is significantly larger than the ~2°C proposed by the *Climate: Long-Range Investigation, Mapping, and Prediction* (*CLIMAP*) *Project* [1981] as well as by other studies [*Broecker*, 1986; *Lyle et al*., 1992]. Atmospheric general circulation models (GCMs) with specified sea surface temperatures (SSTs) have had some success in simulating the cold continental climates that have been inferred from proxy data [*Gates*, 1976a, b; *Manabe and Hahn*, 1977; *Kutzbach and Wright*, 1985; *Rind and Peteet*, 1985; *Hall et al*., 1996]. In such experiments, SST is imposed according to CLIMAP reconstructions, and so feedbacks between the atmosphere and the oceans are precluded. Such feedbacks are believed to be quite important, however, in governing today's climate, given their role in determining the mean state of the tropical oceans as well as in interannual and decadal climate variability.

A first step toward modeling such feedbacks was made by incorporating a thermodynamic mixed layer ocean model into an atmospheric GCM [e.g., *Manabe and Stouffer*, 1980], thereby allowing the model to determine SST through a balanced thermodynamic budget while neglecting ocean dynamics. This model was configured for the LGM, and the predicted SSTs were compared to CLIMAP reconstructions [*Manabe and Broccoli*, 1985a, b; *Broccoli and Manabe*, 1987; *Broccoli and Marciniak*, 1996]. In general, these models attain a favorable degree of cooling in the northern high-latitude oceans, but cooling near western boundary currents such as the Kuroshio and the Gulf Stream is, according to the CLIMAP reconstructions, underestimated. Model results show a modest 1–2.5°C cooling of the tropics [*Broccoli and Marciniak*, 1996], although another simulation with modern ocean heat transport imposed delivered cooler tropical temperatures through a water vapor feedback [*Webb et al*., 1997].

In contrast to the CLIMAP results, more recent estimates of glacial tropical climate derived from such varied sources as coral [*Guilderson et al*., 1994], pore fluids [*Schrag et al*., 1996], glacial groundwater [*Stute et al*., 1995], snowline depressions [*Rind and Peteet*, 1985], tropical ice cores [*Thompson et al*., 1995], and pollen records [*Colinvaux et al*., 1996] indicate a ~4–6°C cooling. It is possible that discrepancies among data extracted from different geographical locations may simply reflect a degree of spatial variability in the temperature anomaly field. In particular, the spatial structure of the thermocline in the upper oceans, where it outcrops and where it is deepest, may have been different during the LGM. Determining the morphology of the glacial thermocline is therefore a crucial step toward reconciling the apparently discrepant SST proxy data [*Ravelo et al*., 1990; *Andreasen and Ravelo*, 1997]. In order to do this, it is necessary to explicitly include ocean dynamics in the methodology.

Recently, *Weaver et al*. [1998] used a coupled model that consisted of an ocean GCM coupled to an energy-moisture balance atmosphere. They concluded that the ocean circulation in their model did not contribute to tropical LGM cooling sufficiently to produce the temperature depressions suggested

Copyright 1999 by the American Geophysical Union.

Paper number 1999JD900447.
0148-0227/99/1999JD900447$09.00

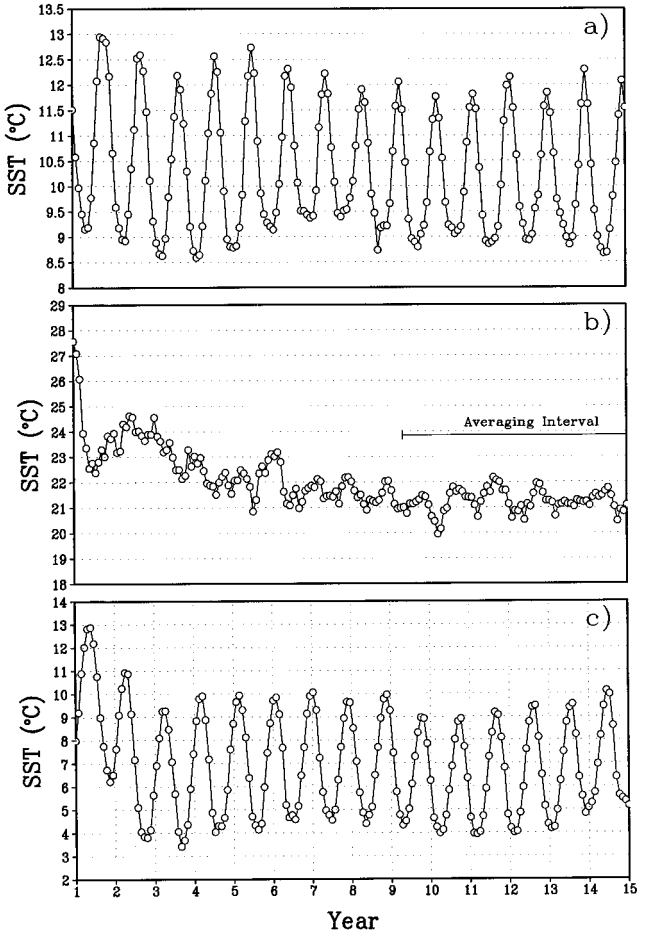

Figure 1. Time series of sea surface temperature (SST) averaged between 180°E and 220°W at (a) 45°S, (b) the equator, and (c) 45°N. The interval over which variables have been averaged for subsequent figures is shown in Figure 1b.

by the recent proxy data. However, analyses of planktonic foraminifera indicate a steeper tilt of the equatorial Pacific thermocline during glacial times, with isotherms shoaling more in the east and deepening more in the west [*Andreasen and Ravelo*, 1997]. Such a change suggests enhanced easterly trade winds over the Pacific and would be consistent with inferred increases in upwelling indices and eolian deposits [*Pedersen*, 1983]. In general, proxy data do suggest a stronger atmospheric circulation during glacial periods [e.g., *Parkin and Shackleton*, 1973; *Pedersen*, 1983; *Sarnthein et al*., 1981; *Molina-Cruz*, 1977]. Therefore, in addition to thermodynamical coupling, dynamical coupling between the atmosphere and the ocean may be equally important in determining LGM climate.

This paper presents the results of a decadal simulation of a coupled atmosphere-ocean GCM which has been configured for the LGM. A decadal simulation is relevant to the above issues because the dynamics of the atmosphere, the thermocline, the upper ocean, and sea ice work on and below this timescale. In particular, since the tropics represent a third of the surface area of the planet, emphasis is placed on the wind-driven dynamics which regulate tropical SST. This is not to say, however, that the dynamics of deep ocean currents are unimportant (although the results of *Weaver et al*. [1998] suggest that the thermohaline circulation does not contribute to LGM tropical cooling). Rather, emphasis is placed primarily on upper ocean dynamics in the determination of SST (and hence the climate) since the dynamics of the coupling between the deep ocean and the surface ocean are still poorly understood [e.g., *Pedlosky*, 1996]. The outline of the paper is as follows: the model is described in section 2, the results are presented in section 3, and a discussion and conclusion follow in section 4.

2. Model

The atmospheric component of the model is the spectral atmospheric GCM of the Geophysical Fluid Dynamics Laboratory (GFDL) [*Gordon and Stern*, 1982]. Rhomboidal truncation at wavenumber 30 is applied in the horizontal, and there are 14 unevenly spaced σ levels in the vertical at σ = 0.015, 0.05, 0.101, 0.171, 0.257, 0.355, 0.46, 0.568, 0.676, 0.777, 0.866, 0.935, 0.979, and 0.997 (where σ, a normalized pressure coordinate, is defined by $\sigma = P/P^*$, with P^* equal to the spatially and temporally varying surface pressure). Atmospheric CO_2 levels are set to 200 ppm and are assumed to be spatially uniform; the distribution of ozone is kept the same as today's. Clouds are predicted according to the scheme of *Wetherald and Manabe* [1988], with stratus clouds calculated separately according to the scheme of *Philander et al*. [1995]. Seasonal, but not diurnal, solar insolation is imposed with the orbital parameters of obliquity, eccentricity, and longitude of perihelion set for 21 ka [*Berger*, 1992]. Ice sheet topography for 21 ka [*Peltier*,

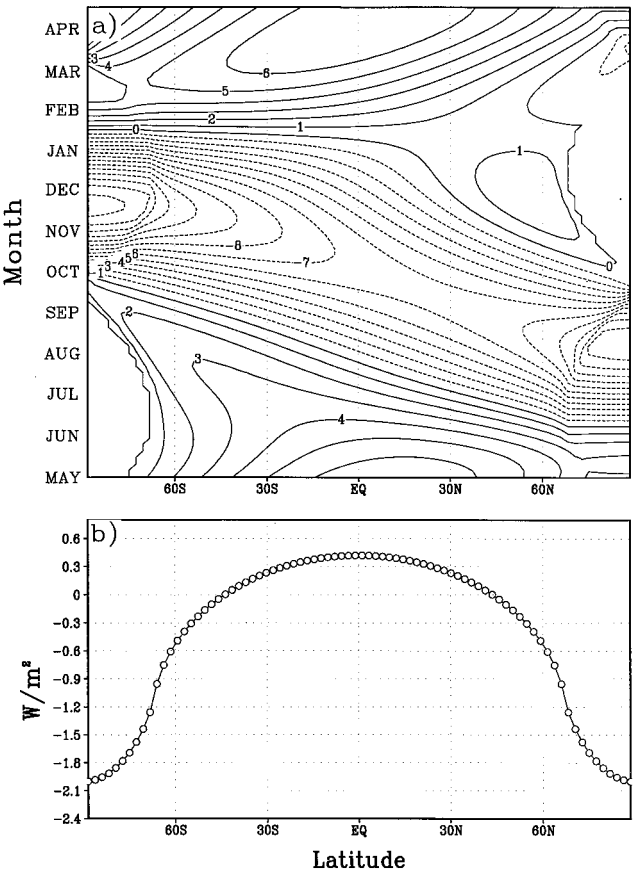

Figure 2. (a) Difference in insolation (in W m^{-2}) as a function of latitude and time (Last Glacial Maximum (LGM) minus present day). (b) Difference in annual mean insolation (W m^{-2}).

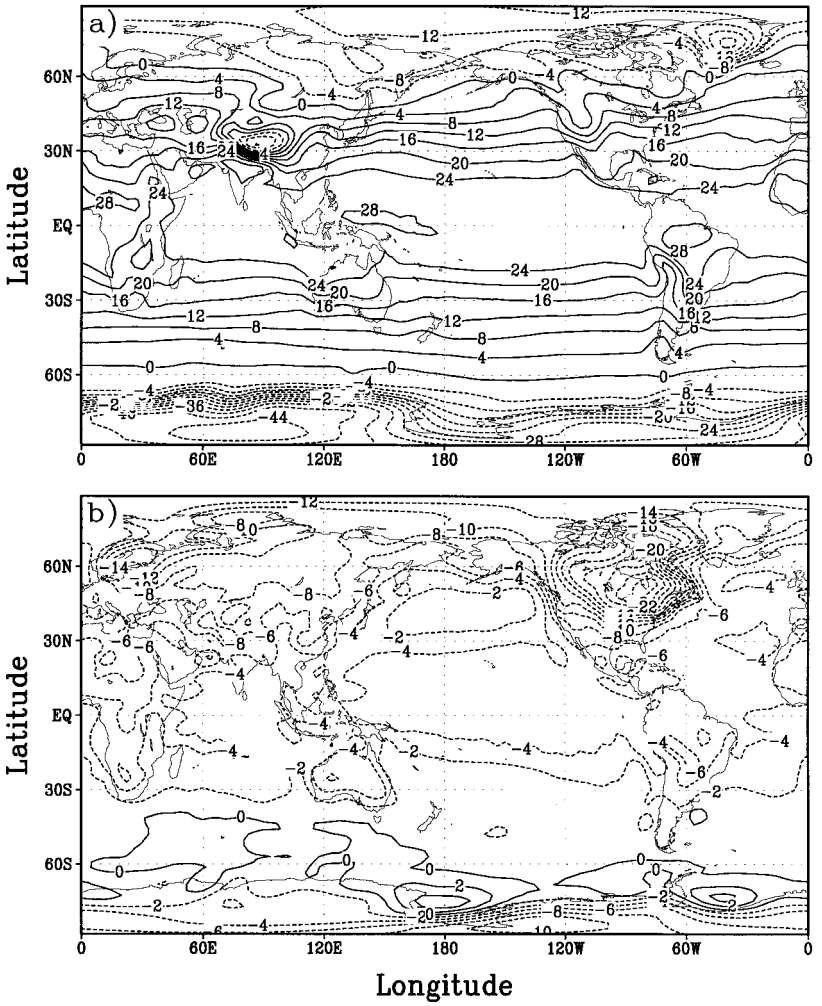

Figure 3. (a) Annual mean near-surface temperature (on the $\sigma = 0.997$ level) in the present-day simulation. (This level corresponds roughly to 30 m above ground in a standard atmosphere.) (b) The difference (LGM minus present day) in annual mean temperature. Contour interval is 4°C in Figure 3a and 2°C in Figure 3b.

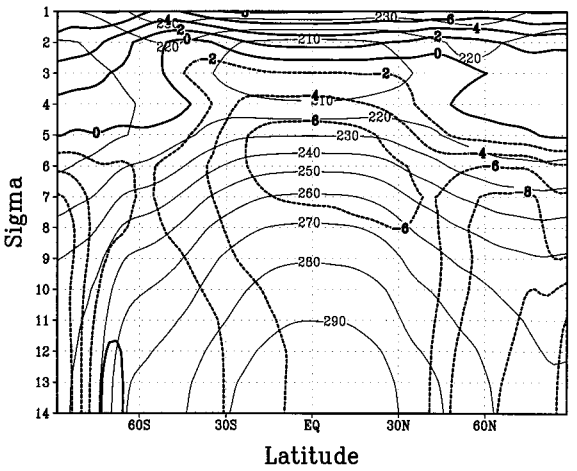

Figure 4. Annual and zonal mean temperature in the present-day simulation (in °K) as a function of latitude and height (in σ coordinates). Departures from this in the LGM simulation are indicated by the thick line (in °K).

1994] is spectrally decomposed then truncated at wavenumber 30 with the aid of an isotropic spectral smoothing to reduce Gibbs oscillations [*Navarra et al*., 1994]. In those spatial locations where presently there are sharp mountains (e.g., the Rockies) but which, at the LGM, were covered by a comparatively flat ice sheet, gravity wave drag is set to zero. Bare land surface albedo for the LGM [*CLIMAP*, 1981] is imposed but may be modified during the integration by snowfall.

The oceanic component of the model is GFDL's Modular Ocean Model, a three-dimensional primitive equation GCM [*Bryan*, 1969; *Pacanowski et al*., 1991]. The governing equations are cast in finite difference form with the addition of ∇^4 horizontal diffusion and, since the model domain is global, additional smoothing in high latitudes where grid boxes converge. Vertical mixing is based on a Richardson number scheme [*Pacanowski and Philander*, 1981]. The spatial resolution of the ocean model is 2° in latitude and 3.62° in longitude, with 15 unevenly spaced levels in the vertical. Bathymetry and coastlines are imposed assuming an LGM sea level that is 120 m lower than today's [e.g., *Fairbanks*, 1989]. Sea ice location and

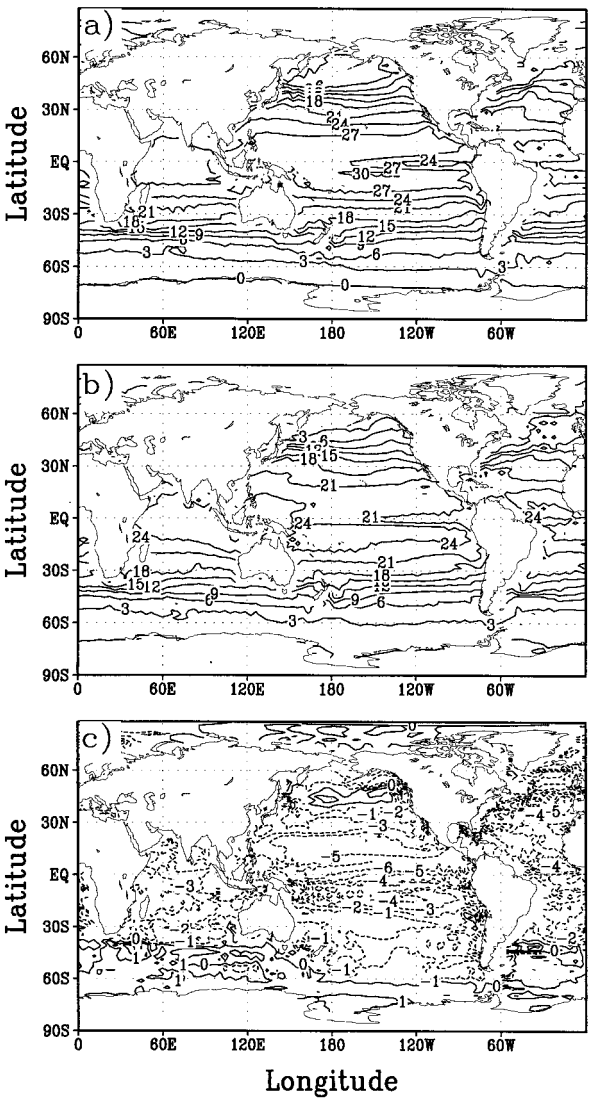

Figure 5. Annual mean sea surface temperature (in °C) for (a) the present day, (b) the LGM, and (c) the difference (LGM minus present day). Contour intervals are 3°C in Figures 5a and 5b and 1°C in Figure 5c.

amount are calculated according to the thermodynamic formulation of *Fanning and Weaver* [1996], which includes brine rejection. The ice model communicates with both the atmospheric and oceanic models and performs flux balances at the top and bottom of the ice with an assumed thermal diffusion within the ice itself. The albedo of sea ice is calculated according to ice thickness and surface temperature. If ice is thicker than 1 m, then its albedo is 0.8 (if the surface temperature is <263.16°K) or 0.55 (if the surface temperature is 273.16°K). A linear interpolation between these albedo values is performed for intermediate temperatures. If ice is thinner than 1 m, then a linear interpolation is made between the albedo of water at that latitude and the albedo calculated according to the above procedure. The ocean is initially at rest with temperature and salinity fields specified from Levitus data [*Levitus*, 1982].

The models are integrated asynchronously with a 1-day integration interval. The coupling scheme provides dynamical and thermodynamical communication between the models at the end of these integration intervals. The atmosphere receives from the ocean the daily mean SST and surface current velocities. The ocean receives from the atmosphere the daily mean vector components of wind stress, net heat flux, net freshwater flux, and net shortwave radiation.

Results from a 15-year LGM simulation are compared to those from a 40-year present-day simulation. No flux correction is applied during the course of these integrations since the present-day simulation reproduces observed climatology quite well over this decadal time period (see next section). The largest discrepancy between the present-day simulation and observations occurs in the regions where semipermanent stratus clouds exist, such as in the eastern equatorial Pacific south of the equator. Despite the model's stratus parameterization, cloud amount in these localized regions is underpredicted and leads to warmer SST than is observed.

In subsequent figures, quantities from the LGM simulation have been averaged over the last 5 years of the integration after the adjustment of the upper ocean to the glacial atmospheric forcing (Figure 1). Since the control simulation has been integrated for a longer time, the "present-day" quantities have been averaged over the last 23 years of the integration.

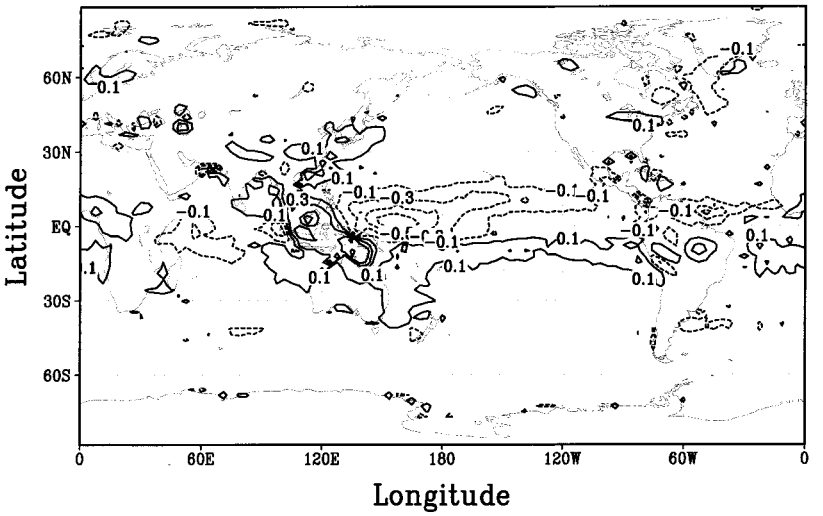

Figure 6. Difference in annual mean net freshwater flux (precipitation minus evaporation) between the two simulations (LGM minus present day). Contour interval is 0.2 cm d^{-1}.

Table 1. Annual Mean Precipitation (P), Evaporation (E), Runoff Rate (P − E), Aridity Index (E/P), Runoff Ratio ((P − E)/P), and Water Equivalent Snow Amount (S) for the Present-Day Simulation

	P, cm d^{-1}	E, cm d^{-1}	P − E	E/P	(P − E)/P	S, cm
	0.2459 (0.2206)	0.2421 (0.2150)	0.0039 (0.0056)	0.984 (0.975)	0.0159 (0.0253)	1.01 (1.52)
45°N–90°N	0.1935 (0.1508)	0.0965 (0.0681)	0.0970 (0.0827)	0.4989 (0.4517)	0.5010 (0.5483)	3.16 (6.28)
0°N–45°N	0.2711 (0.2135)	0.2928 (0.2562)	−0.0217 (−0.0427)	1.0802 (1.1998)	−0.0802 (−0.1997)	0.09 (0.29)
20°S–20°N	0.3603 (0.3089)	0.3751 (0.3233)	−0.0148 (−0.0144)	1.0410 (1.0466)	−0.0411 (−0.0466)	0.0 (0.0)
45°S–0°N	0.2680 (0.2774)	0.3181 (0.2886)	−0.0502 (−0.0112)	1.1872 (1.0404)	−0.1872 (−0.0404)	0 (0)
90°S–45°S	0.1865 (0.1722)	0.0863 (0.0893)	0.1002 (0.0829)	0.4628 (0.5187)	0.5372 (0.4813)	3.45 (3.26)

Values in parentheses are for the Last Glacial Maximum simulation averaged over the globe and along the latitude belts shown.

3. Results

As in the LGM simulation of *Hall et al*. [1996] and *Weaver et al*. [1998], orbital parameters for 21 ka are imposed. The difference between 21 ka and present-day insolation indicates that in latitudes above 60°N, LGM insolation between early June and October is smaller by up to 10 W m^{-2} and is greater by ~4 W m^{-2} between April and early June (Figure 2a). In the tropics and subtropics (30°N–30°S), LGM insolation is greater by up to 6 W m^{-2} between January and July and smaller by up to 8 W m^{-2} between July and January. The Southern Hemisphere has less insolation, by up to 14 W m^{-2}, between October and mid-January and more insolation, by up to 5 W m^{-2}, between mid-January and October [see also *Kutzbach and Guetter*, 1986].

The difference in annual mean insolation (Figure 2b) demonstrates that at 21 ka, slightly more insolation is received equatorward of 45°N and 45°S (with a maximum difference of 0.42 W m^{-2} on the equator) and less insolation is received poleward of 45°N, 45°S (up to 2 W m^{-2} less). While the annual mean values represent <1% change in insolation, they are significant, given the fact that the changes in global mean net radiative forcing caused by glacial values of continental ice, atmospheric CO_2, and bare surface albedo are of the order of 1 W m^{-2} [*Broccoli and Manabe*, 1987]. Seasonal values, on the other hand, represent a ~2–3% change and are therefore important to such seasonal phenomena as monsoons.

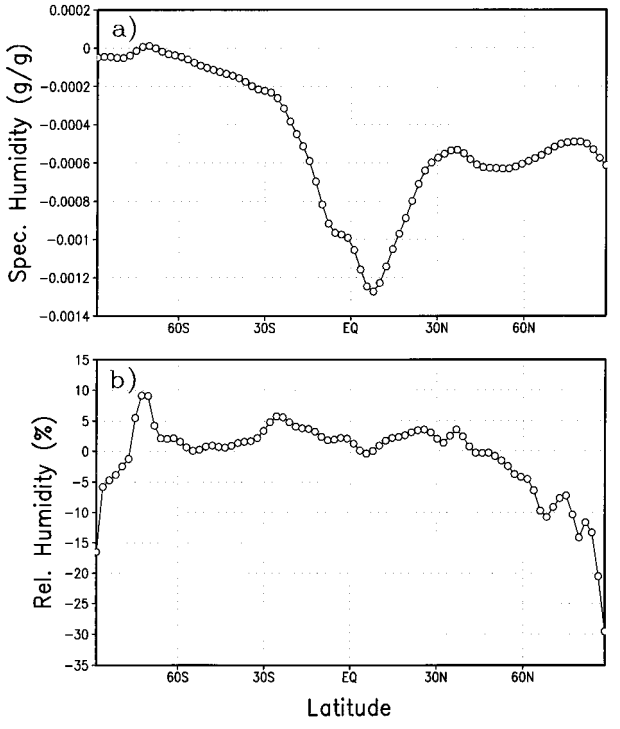

Figure 7. Difference (present day minus LGM) in (a) specific humidity (g g^{-1}) and (b) surface relative humidity (%). The annual mean values of Figure 7a have been averaged vertically and zonally, and in Figure 7b they have been averaged zonally.

These differences in annual mean insolation enhance the meridional baroclinic structure of the LGM atmosphere as indicated by the near-surface atmospheric temperature (Figure 3). There is a much greater cooling of the poles than of the tropics, particularly in the Northern Hemisphere, where the continental ice volume is greatest (Figure 3b). Differential cooling of the Northern and Southern Hemispheres was also noted by *Manabe and Broccoli* [1985a] and *Hyde et al*. [1989]. Interior Antarctic temperatures are, nevertheless, up to 11°C colder. Annual mean temperature depressions over Southern Hemisphere landmasses are typically 4°–6°C. Two regions of warmer LGM temperatures in the high southern latitudes are the result of a local reduction in sea ice amount (see section 3.6).

The global mean difference (LGM minus present day) in simulated near-surface temperature is −4.3°C in an annual mean, −5.4°C in a December-January-February (DJF) mean, and −2.8°C in a June-July-August (JJA) mean. The relatively large contrast in seasonal cooling between Northern Hemisphere winter and summer is caused by the ice sheets themselves, which induce stronger wintertime cooling by enhancing the snow-albedo feedback.

The annual mean, zonally averaged tropospheric cooling in the LGM simulation extends from the surface throughout the troposphere, enhancing particularly the northern midlatitude baroclinicity (Figure 4). The temperature difference also indicates a warmer stratosphere. High northern latitudes exhibit the largest degree of cooling because of the ice sheets themselves, with secondary maxima over Antarctica and in the upper equatorial troposphere (where there is reduced latent heating). The spatial pattern of this cooling is quite similar to that produced with the NASA/Goddard Institute for Space Studies (GISS) GCM [*Rind and Peteet*, 1985], although the magnitude is larger here by a factor of nearly 2.

Annual mean sea surface temperature depressions indicate a ~3–4°C cooling over much of the glacial oceans (Figure 5). There is above average cooling, reaching 6°C, in the western equatorial Pacific and underneath the present-day Intertropical Convergence Zone (ITCZ). In the North Atlantic near the Gulf Stream, cooling reaches 9°C at 40°N. Below average cooling is found in the subtropics and midlatitudes of the Pacific Ocean and in the Southern Ocean. Cooling in the Southern Hemisphere is largely consistent with the CLIMAP reconstructions.

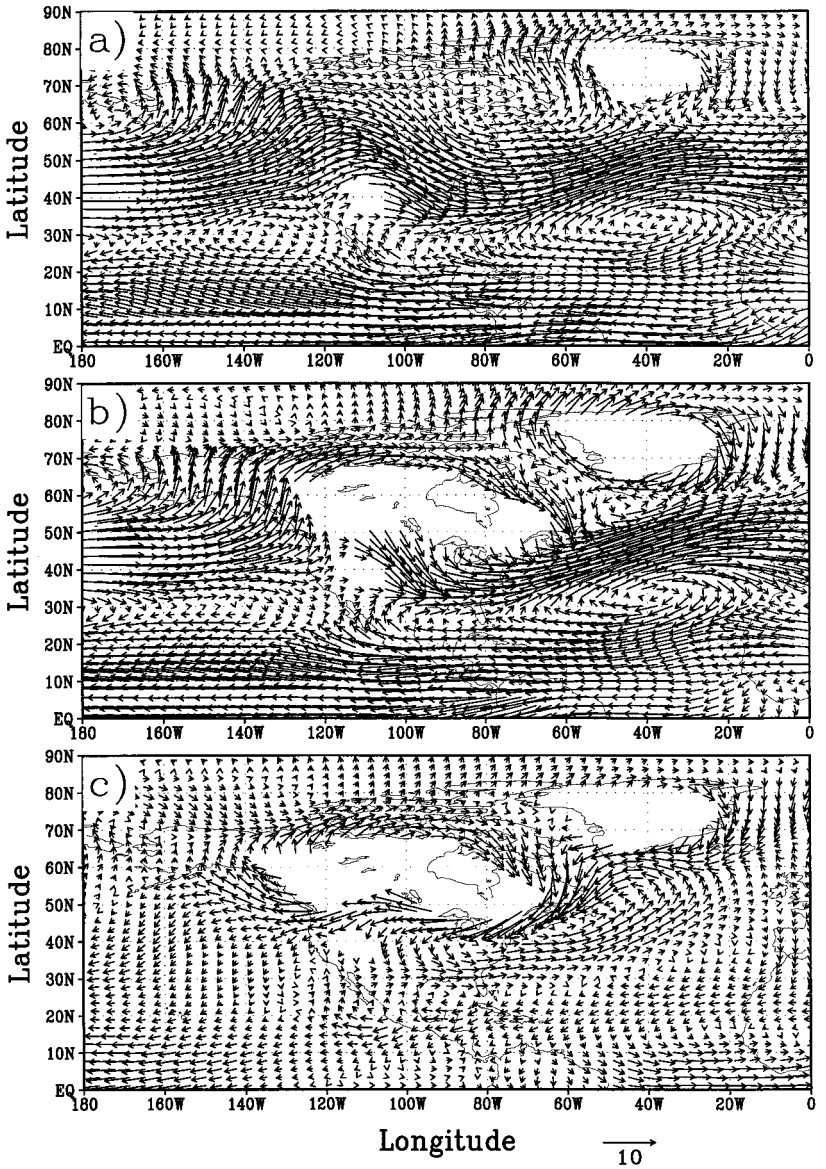

Figure 8. Annual mean 850-mbar winds over North America for (a) the present day, (b) the LGM, and (c) their difference (LGM minus present day). No vectors are plotted where the 850-mbar surface is below topography. Units are m s^{-1}, and vectors are scaled according to the vector displayed at bottom right.

Above the regions of strong SST cooling there is a large decrease in the net freshwater flux (precipitation minus evaporation), particularly over the western equatorial Pacific (Figure 6). Differences in this region are attributed primarily to precipitation changes: there is a substantial decrease in precipitation over the western warm pool and in the ITCZ, and there is a precipitation increase over the Indonesian archipelago and along the South Pacific Convergence Zone (SPCZ). Global mean precipitation and evaporation both decrease by ~11%, indicating a reduction in the global hydrological cycle (Table 1). The zonal mean aridity index E/P [e.g., *Piexoto and Oort*, 1992] indicates more arid conditions in the high northern latitudes but ~10% less arid conditions in the low northern latitudes as well as in the high southern latitudes. LGM snowfall is consistently greater in the Northern Hemisphere and has a global mean value that is ~50% greater.

In the first decade of the LGM simulation during the adjustment toward short-term equilibrium (see Figure 1), an excess of precipitation over evaporation reduces the net amount of atmospheric water vapor. The resulting global mean specific humidity after the adjustment is 10% less than that simulated for the present day. A zonal mean of the vertically averaged specific humidity difference indicates that a majority of the decrease occurs in the tropics (Figure 7a). The lower amount of atmospheric water vapor implies a positive feedback on global cooling. Relative humidity, on the other hand, exhibits slight increases over much of the globe (Figure 7b), decreasing only over the continental ice sheets. This implies that the decrease in saturation specific humidity caused by the atmospheric cooling is larger than the decrease in the actual specific humidity in many regions. Lapse rates in the glacial climate are smaller in the lower troposphere of the Southern Hemisphere subtropics, which implies a lower lifting condensation level and a lowering of snowlines.

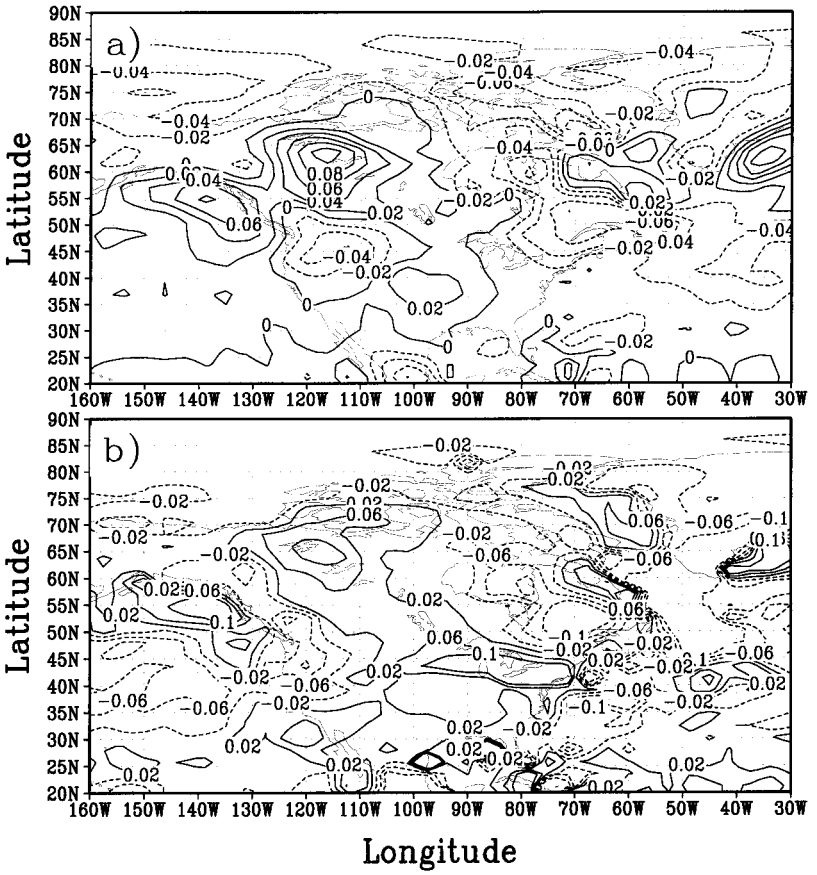

Figure 9. Annual mean difference (LGM minus present day) of North American (a) vertically averaged cloud amount (where a 1 indicates complete cover) and (b) net freshwater flux (the contour interval is 0.04 cm d^{-1}).

3.1. North America and the North Atlantic

In addition to cooling the lower troposphere over North America, the Cordilleran and Laurentide ice sheets reshape the structure of the annual mean winds (Figure 8). At the 850-mbar level, cold temperatures above the ice sheets induce anticyclonic circulations (Figure 8c). Strong westerly flow over the Canadian Arctic (~70°N) arises from a northward redirection of the midlatitude jet by the Cordilleran ice sheet (a blocking which also reduces the strength of the westerlies over the eastern North Pacific). Despite the anticyclonic circulation around the ice sheet margin, the southwesterly jet extending into the north central Atlantic from the southeastern seaboard is stronger by up to 50% (representing a 4.5 m s^{-1} increase) and doubles the rate of evaporation over the far western Atlantic to ~5 cm d^{-1}. In the LGM simulation, the core of this storm track jet is displaced southward by ~3° and its baroclinicity (as measured by the vertical wind shear at 50°W) is 26% greater. In combination with the northeasterly flow along the southeastern edges of the Laurentide and Greenland ice sheets, this storm track jet produces a strong cyclonic circulation south of Greenland, east of Newfoundland.

Changes in the annual mean (vertically integrated) cloud cover and net freshwater flux indicate that regions of the North American interior experience cloudier and wetter conditions in the LGM simulation, while others are clearer and drier (Figure 9). Increased cloud cover and precipitation occur along the northwestern margin of the Cordilleran ice sheet where there is topographic redirection and uplift of the midlatitude westerly jet. Dry, sinking air in the anticyclonic circulation along the eastern margin of the Laurentide ice sheet decreases cloud amount along much of the northeastern seaboard. Along the southeastern seaboard, however, the freshwater flux reaches 0.15 cm d^{-1} greater than the 0.1 cm d^{-1} simulated for the present day.

A broad band of increased freshwater flux extends from the Great Lakes southwest across the central United States to the Baja peninsula, with typical values being 0.025 cm d^{-1} greater (representing a ~20% increase). Combined with a 6°–10°C annual mean cooling, this result agrees well with proxy data for the region [*Peterson et al.*, 1979]. Along the far western coasts of the United States and southern Canada there is a ~30% decrease in freshwater flux because of the northward redirection of the midlatitude jet. Evidence for glacial aridity in this region comes from the Cascade range, where data indicate that a cold, dry steppe vegetation was present near 45°N, 120°W [*Whitlock and Bartlein*, 1997].

Increased precipitation underneath the North Atlantic storm track increases the freshwater flux over most of the Atlantic Ocean, decreasing LGM sea surface salinity (SSS) by up to 1.5 (Figure 10a). Over the far western Atlantic the stronger LGM winds evaporate the surface waters sufficiently that there is a slight (~0.2) salinity increase. Additionally, North Atlantic SST (Figure 10b) indicates that the LGM Gulf Stream is more zonal and thereby prevents the advection of

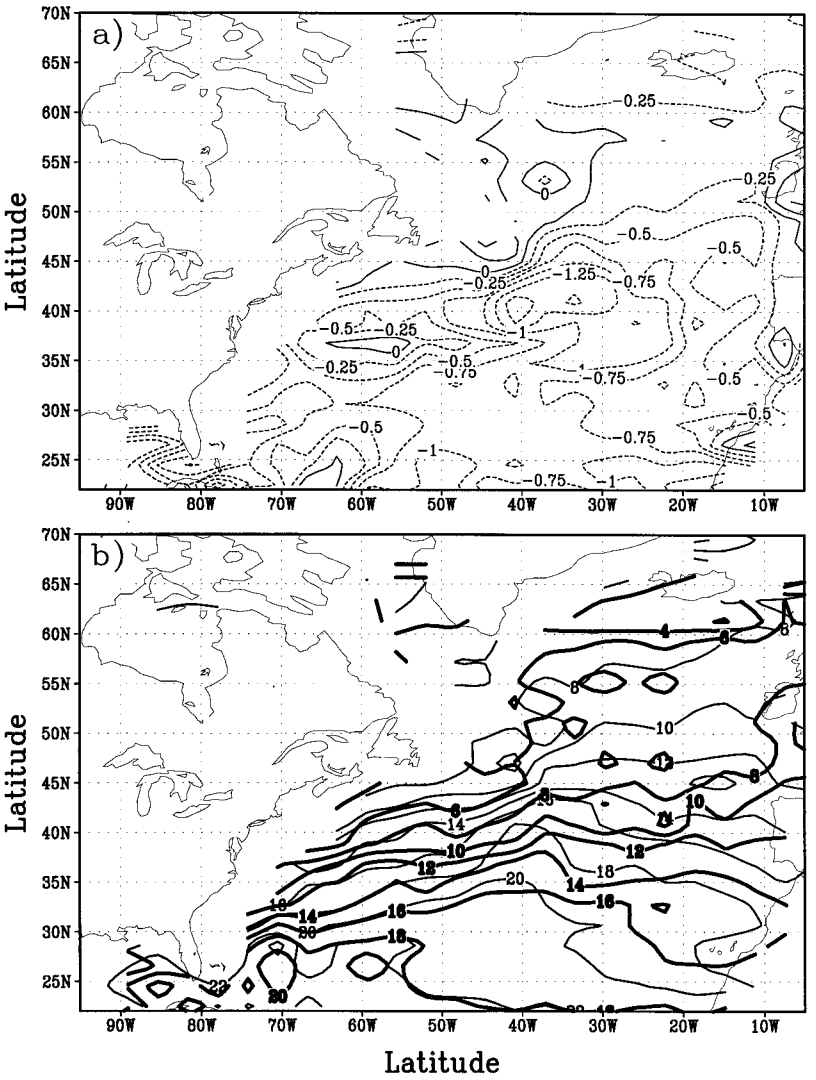

Figure 10. (a) Annual mean difference in sea surface salinity (LGM minus present day) in the North Atlantic, in practical salinity units. (b) Annual mean sea surface temperatures (°C) for the present day (thin contours) and for the LGM (thick contours). The contour intervals are 0.25 psu in Figure 10a and 2°C in Figure 10b.

high subtropical salinities into the north central Atlantic. The greatest simulated SST cooling is 9°C near 40°W, 40°N and arises primarily from the altered flow path of the Gulf Stream (as opposed to a direct radiative cooling), which in turn is caused by the altered wind stress forcing of the North Atlantic storm track jet. CLIMAP estimates indicate a maximum of ~12°C cooling in the vicinity of the Gulf Stream and an 8–12°C cooling over much of the northeastern Atlantic; the latter cooling is not captured in this simulation.

3.2. Eurasia

Over the Fennoscandian, Barents, and Kara ice sheets there is an anticyclonic flow around the ice margins which weakens the westerly trade winds over the Asian interior by up to 3.5 m/s (representing a 70% decrease in some regions; see Figure 11). Net freshwater flux over north central Asia (~40°E–140°E, 50°N–75°N) is reduced by 50% since this anticyclonic circulation draws dry Arctic air southward into the continental interior where annual mean temperatures are 8°–12°C colder than present (see Figure 3).

The westward shift of glacial "tropical" convection to the region above the Indonesian archipelago is evident in the vector wind difference (Figure 11c). Increased surface convergence over this region is concomitant with stronger easterlies over the western Pacific and stronger westerlies over the Indian Ocean. The westerly summer monsoon winds increase in strength, despite the fact that there is a much larger snow deposit over the Tibetan Plateau (a ~25% increase in area of annual mean snow cover; see Figure 12). Maximum 850-mbar jet speeds in the monsoon occur over the Bay of Bengal in both simulations with the LGM value (~14 m/s) nearly double that of the present day.

Despite stronger subtropical monsoon westerlies, equatorial easterlies over the Indian Ocean are substantially weaker. Evaporation over the Indian Ocean and southwesterly moisture flux into the monsoon are reduced. Consequently, JJA freshwater flux over the south Arabian Sea and much of the northwestern Indian subcontinent is reduced (Figure 13). Stronger subtropical westerlies, however, increase simulated

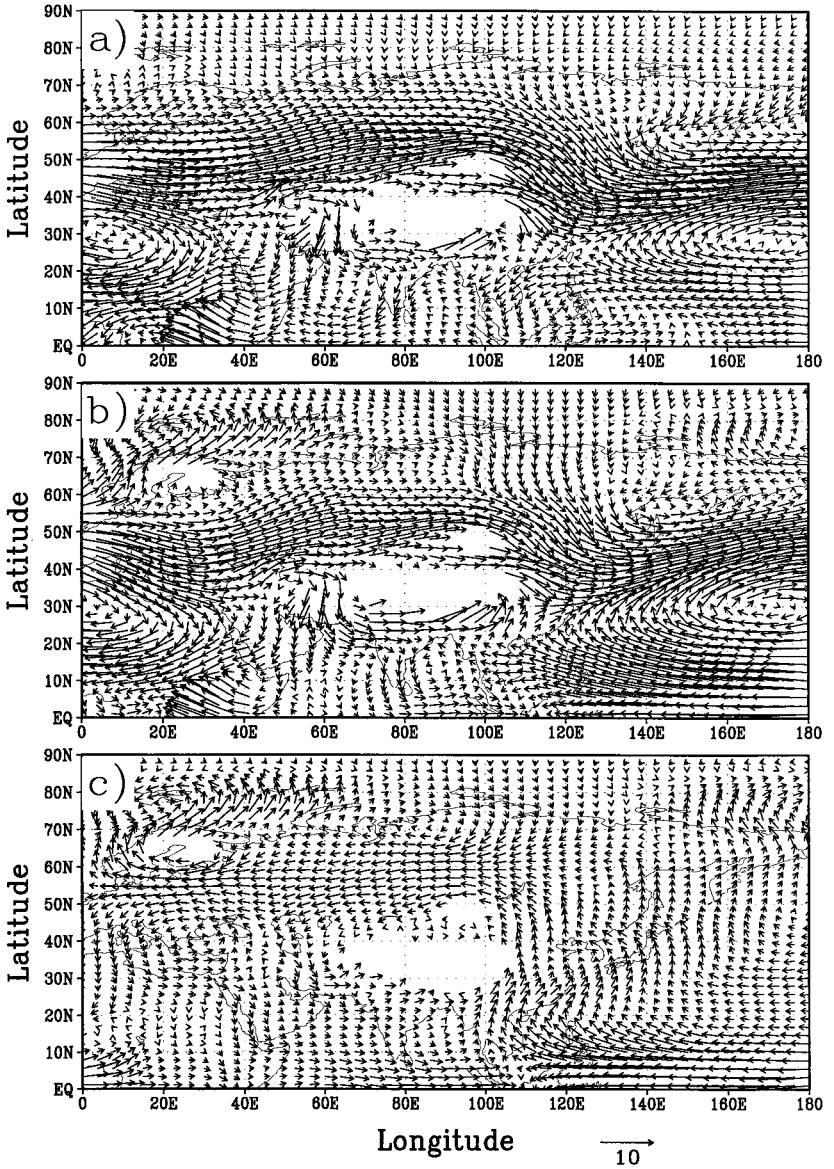

Figure 11. Annual mean 850-mbar winds over Eurasia for (a) the present day, (b) the LGM, and (c) LGM minus present day. Units are m s^{-1}, and vectors are scaled as shown.

precipitation and freshwater flux farther to the east over China and Thailand.

3.3. Africa

Increased annual mean cloud cover over western equatorial Africa and south Africa enhances continental cooling in these regions (Figure 14). In an annual mean, LGM temperatures over equatorial Africa can be 7°–8°C colder (Figure 14b). The vector difference in 850-mbar winds arises predominantly from JJA changes, when the pressure field induced by differential cooling of the continental interior increases the westerly monsoon flow over the sub-Saharan region (Figure 14b). Stronger LGM African monsoon winds weaken the mean easterlies over the equatorial Atlantic and increase the net freshwater flux over the Nigerian region by up to 1 cm d^{-1} in a JJA mean and up to 0.3 cm d^{-1} in an annual mean (Figure 14c).

Geological evidence for weaker easterly winds over this region of the Atlantic comes from analyses of eolian deposits near 20°N off the west coast of Africa. *Sarnthein et al*. [1981] have estimated that, during the LGM, easterlies weakened from 8 to 5 m s^{-1}, offshore upper level southeasterly flow weakened from 20–25 to 12 m s^{-1}, and northerly alongshore flow strengthened from 14 to 20 m s^{-1}. As dust transport and settling occurs predominantly in the wake of east African waves, which arise during the African monsoon season, these differences primarily reflect changes in the JJA winds. A stream function plot of the JJA near-surface winds in the present-day simulation (Figure 15a) indicates that the alongshore trades, the easterly Atlantic trades, and the monsoon westerlies near 10°N are all captured by this model. For the LGM simulation the stream function difference (Figure 15b) indicates weakened easterly trades and enhanced northerly coastal flow in the LGM simulation, in good agreement with the proxy data. Near the coast from 5°N–20°N, LGM winds are ~4 m s^{-1} more westerly, which, in places, represents a 100% change. The northerly coastal flow is ~2 m s^{-1} stronger, rep-

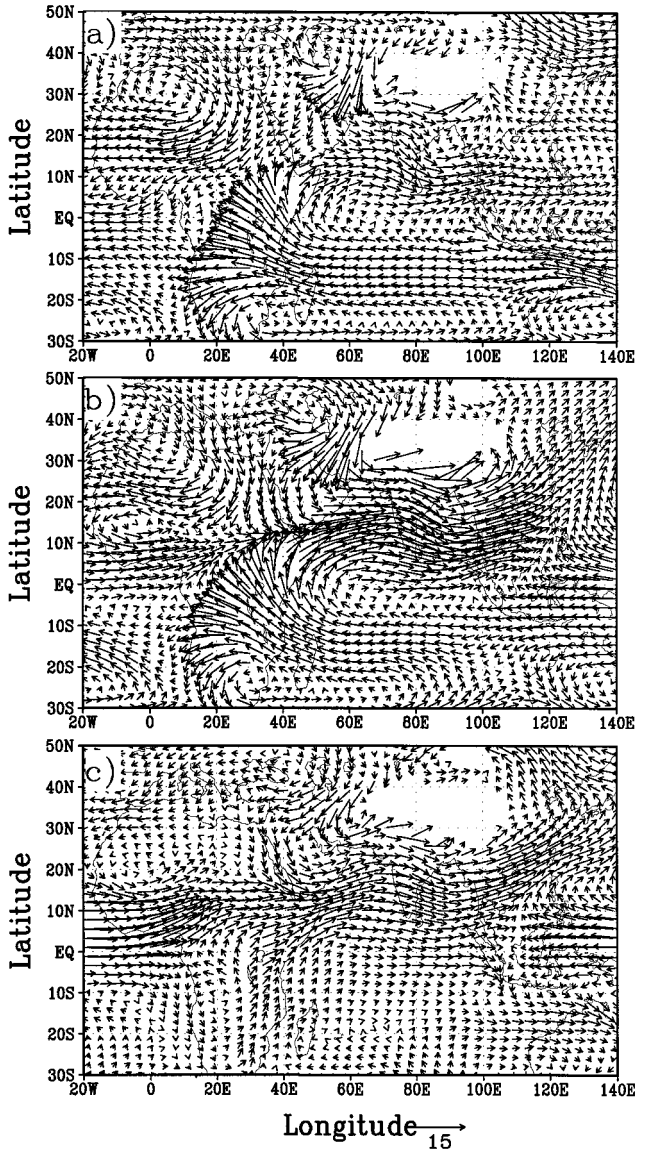

Figure 12. June-July-August (JJA) 850-mbar winds over the south Asian monsoon region for (a) the present day, (b) the LGM, and (c) LGM minus present day. Units are m s^{-1}, and vectors are scaled as shown.

resenting a 25% increase. Higher in the troposphere the stream function difference (Figure 15c) indicates a weakening of the southeasterly offshore flow near 20°N: offshore winds at this level are reduced from 6 m s^{-1} in the present-day simulation to 3 m s^{-1} for the LGM. Changes in African monsoon winds in this LGM simulation therefore appear to be consistent with some of the proxy data.

However, proxy data for moisture in this region tend to indicate drier conditions [*Peterson et al*., 1979], whereas the model indicates wetter conditions. In the central Sahara, simulated annual mean temperatures are 5°–6°C colder and the net freshwater flux is not substantially different. Lake level data from the eastern Sahara indicate, in general, drier conditions [*Peterson et al*., 1979; *Street-Perrott and Harrison*, 1985].

Increased 850-mbar divergence over the East African Highlands decreases the net freshwater flux by 0.02–0.1 cm d^{-1} along the African coast east of Lake Victoria from 20°S–10°N, a region for which proxy data also indicate drier conditions [*Street-Perrott and Harrison*, 1985]. Mean annual temperature depressions in the highlands are up to 7.5°C cooler, with 6°–7°C being typical over high topography. These temperature depressions agree well with those estimated from tree line lowering [*Flenley*, 1979]. *Jolly and Haxeltine* [1997] have demonstrated from simulations performed with the Global biome model (BIOME3) vegetation model that a reconstruction of 6.5°C cooling is reasonable but only if the change is due to temperature and not to a change in vegetation induced by lowered atmospheric CO_2. The bare surface albedos in the LGM simulation are greater in the highlands but only by ~2%, so the simulated temperature change is not driven by the difference in bare surface albedo.

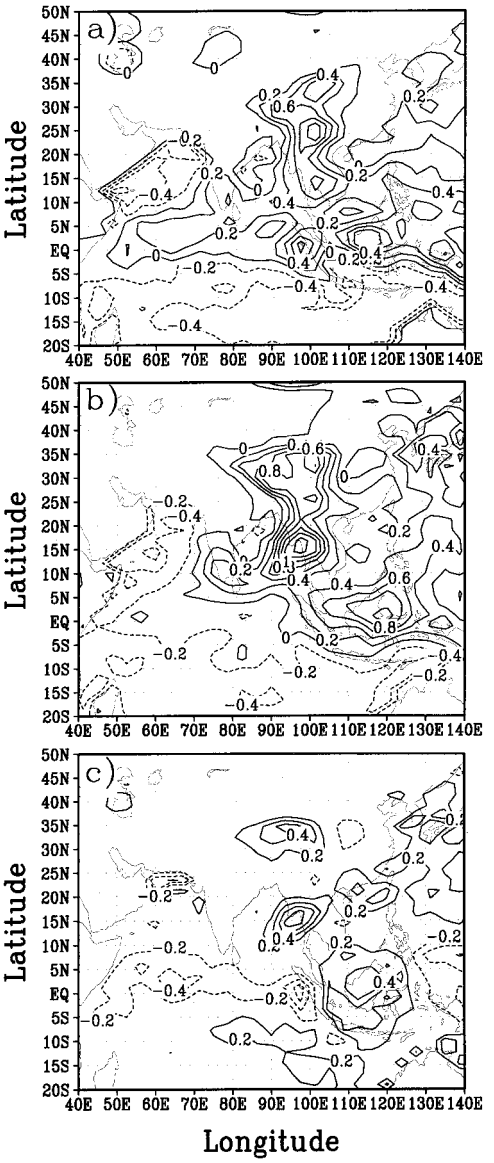

Figure 13. JJA net freshwater flux in the south Asian monsoon for (a) the present day, (b) the LGM, and (c) their difference (LGM minus present day). Contour intervals are 0.2 cm d^{-1} in Figures 13a and 13b and 0.1 cm d^{-1} in Figure 13c.

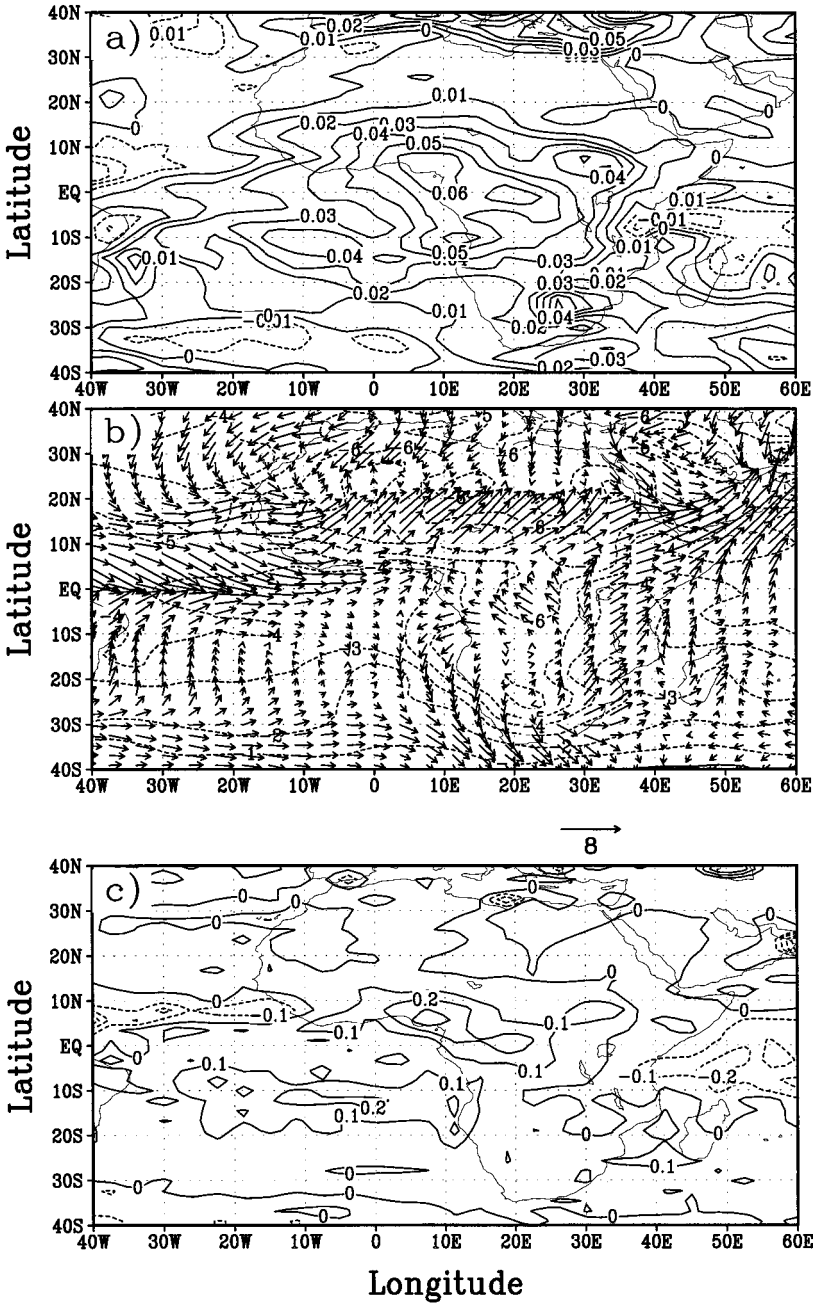

Figure 14. (a) Difference in vertically averaged, annual mean cloud amount over Africa (LGM minus present day; contour interval is 1%). (b) Vector wind difference (LGM minus present day) in JJA near-surface winds (m s^{-1}). Vectors, which are plotted at every other point, are scaled as shown. The difference in annual mean temperature is shown in contours with an interval of 1°C. (c) Difference in annual mean freshwater flux (LGM minus present day; contour interval is 0.1 cm d^{-1}).

3.4. South America

In tropical South America, cooling can reach 7°C near 64°W–13°S with a 4.5°–6°C cooling over much of lowland Brazil (Figure 16a). The magnitude of the average cooling is approximately the same as that predicted from noble gases [*Stute et al.*, 1995] and pollen records [*Colinvaux et al.*, 1996]. In addition to this cooling, there is an increase in relative humidity at the surface of ~10% over much of the continental interior. This result appears to be consistent with vegetational changes in central Brazil, which indicate more humid but cooler conditions [*Salgado-Labouriau et al.*, 1997].

The change in net freshwater flux indicates drier conditions in the north and northwest lowlands but wetter conditions in the central eastern part of the continent along 10°S (Figure 16b). A typical value of the change in freshwater flux is 1 cm d^{-1}. In comparison to data from Lake Pata in northwestern Brazil, which indicate a 5°–6°C cooling and not much change in freshwater flux [*Colinvaux et al.*, 1996], averages over the area

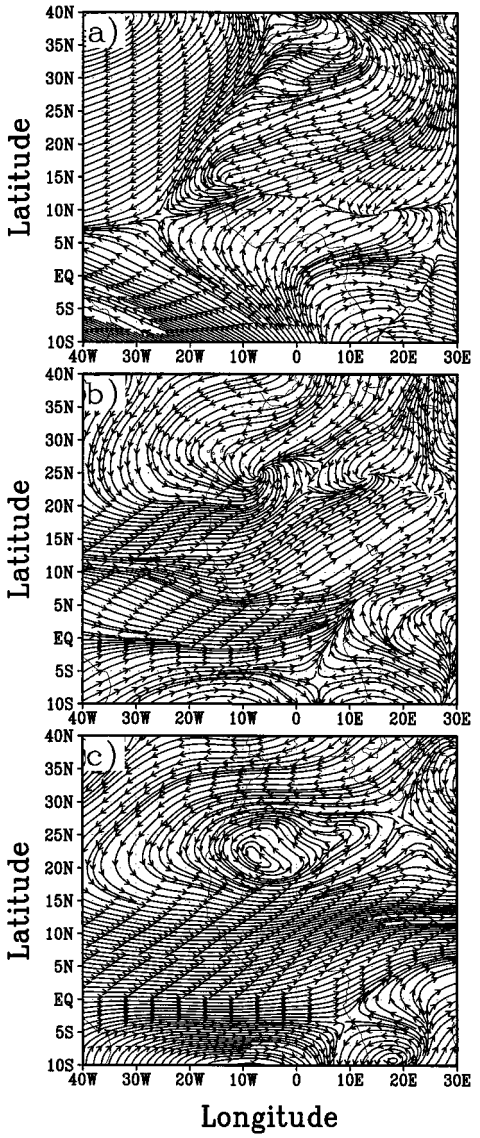

Figure 15. Stream function plots of (a) JJA winds near the surface over west Africa in the present-day simulation, (b) the difference in near-surface winds (LGM minus present day), and (c) the difference in midtropospheric winds (LGM minus present day).

between 68°W–64°W and 2°S–2°N give a 5.2°C cooling and a 17% drying (net freshwater flux in the present-day simulation is 0.44 cm d^{-1} in this region, which compares reasonably well with an estimated 0.38 cm d^{-1} from the climatological observations by *Peixoto and Oort* [1992]).

The vector difference in near-surface atmospheric winds (Figure 16c) indicates enhanced divergence out of the equatorial regions that have cooled the most (such as northeastern Brazil) and increased convergence into the equatorial regions that cool the least (such as coastal Ecuador). The pattern of precipitation changes correlates well with the spatial distribution of these convergent and divergent wind differences.

3.5. Tropical Pacific, Tropical Atlantic, and Sea Ice

Increased easterly trades over the equatorial Pacific Ocean increase both the zonal tilt of the equatorial thermocline and the strength of the Equatorial Undercurrent (Figure 17). The $O(10)$ m changes in thermocline depth in the eastern and western Pacific are reasonable according to the estimates determined from planktonic foraminifera [*Andreasen and Ravelo*, 1997].

Despite the LGM cooling of the upper ocean the temperature at the base of the thermocline is ~12°C in both simulations and occurs at approximately the same depth (~300 m). Given the surface cooling, this implies a reduction in thermal stratification of the LGM thermocline. Of course, if the waters below 300 m were also to cool by ~4°–5°C through processes which are not captured in a decadal simulation (e.g., deep water formation and movement), then the thermal stratification would not be different. However, ocean temperatures below ~1 km are less than 4°C in both simulations and could not, given the limitation imposed by the freezing point of seawater, cool as much as the upper ocean. It is therefore likely

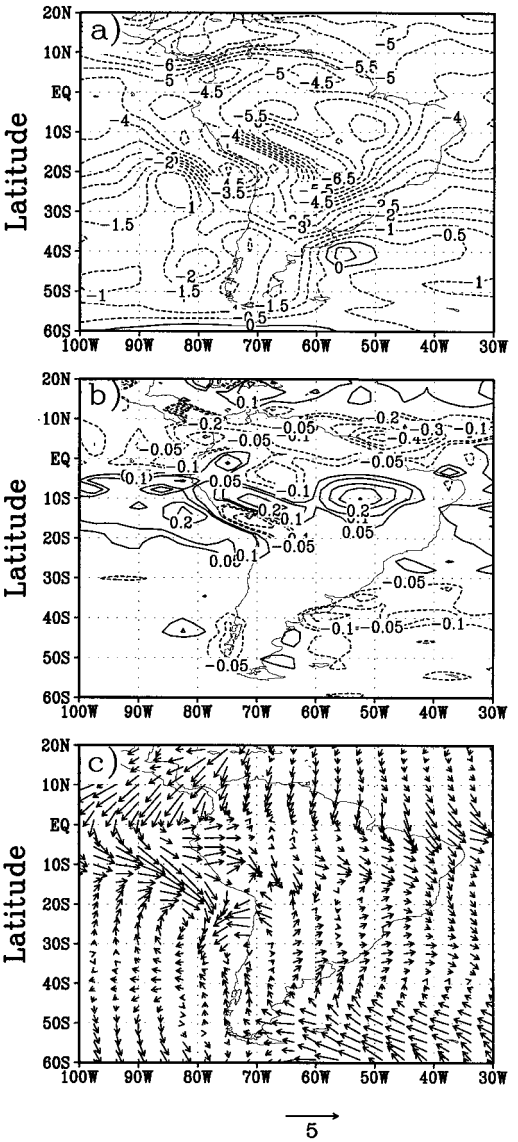

Figure 16. (a) Difference in annual mean temperature over South America (in °C). (b) Difference in freshwater flux (cm d^{-1}). (c) Near-surface vector wind difference (in m s^{-1} with vectors scaled as shown). All differences are LGM minus present day.

that, if the simulated SSTs are reasonable, the thermal stratification of the tropical LGM oceans was reduced.

The latitudes at which the equatorial thermocline outcrops are closer to the equator in the LGM simulation. In a DJF mean the 20°C isotherm outcrops ~4° of latitude closer to the equator and the 18°C outcrops ~2° closer. These values were calculated using a zonal mean SST, where the zonal average is taken over the eastern Pacific subduction zone (150°W–120°W). The differential shifts in the 18°C and 20°C isotherms reflect the reduction in thermal stratification of the subsurface waters.

The 6°C SST cooling in the western equatorial Pacific (Figure 18a) lies underneath the region in which the difference in easterly trade winds is largest (Figure 18b). Westward winds in this area are up to 5 m s^{-1} greater than in the present-day simulation (in which zonal winds are ~0 at 140°E since this is the mean location of tropical convection). Colder SSTs also correlate with a decrease in net freshwater flux (Figure 18c). Over the present-day warm pool the freshwater flux is ~0.6 cm d^{-1}, so the decrease is ~100%. LGM SSS in the western Pacific is therefore greater by ~1, so a typical salinity is 35.

In the equatorial Atlantic Ocean, SST cooling along the equator is ~3.5°C (Figure 19), with slightly stronger cooling

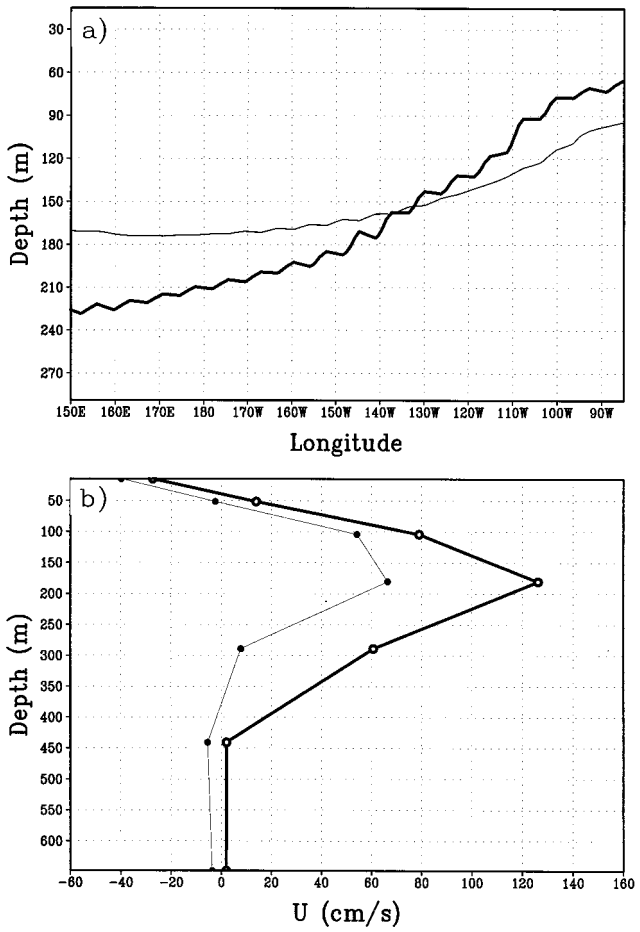

Figure 17. (a) Depth (in meters) of the tropical Pacific thermocline as represented by the 18°C isotherm for the present day (thin line) and the LGM (thick line). (b) Speed (in cm s^{-1}) of the Equatorial Undercurrent as a function of depth taken at 180°W (where the speeds are largest in both simulations) for the present day (thin line) and the LGM (thick line).

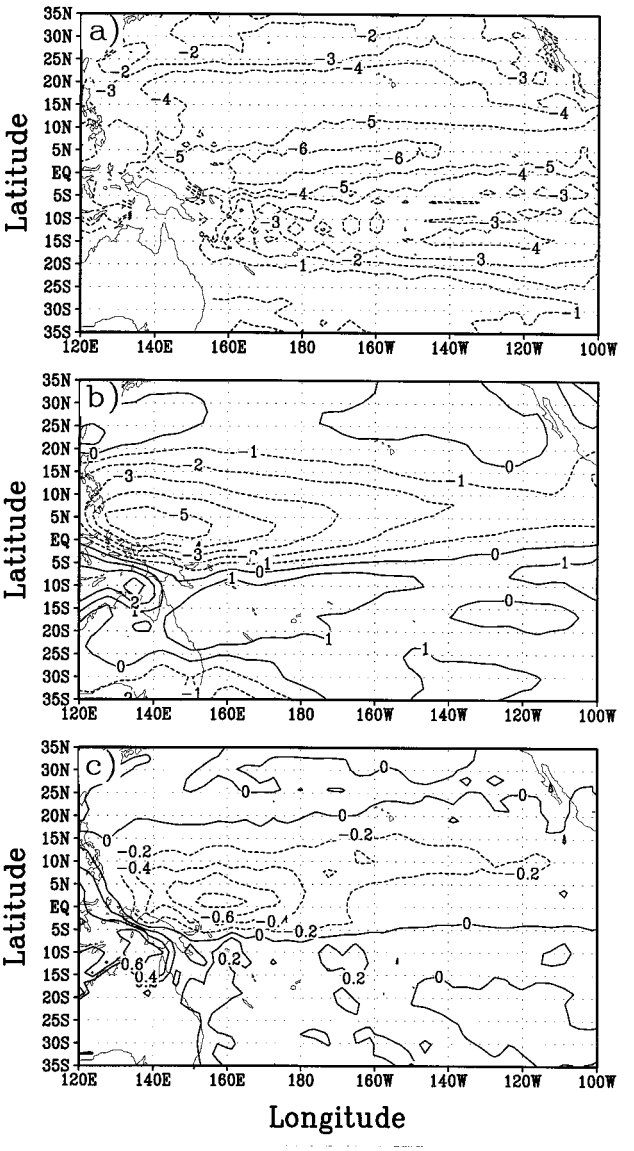

Figure 18. (a) Difference in annual mean SST in the tropical Pacific Ocean (contour interval 1°C). (b) Difference in annual mean zonal atmospheric wind near the surface (contour interval 1 m s^{-1}). (c) Difference in annual mean freshwater flux (contour interval 0.2 cm d^{-1}). All differences are LGM minus present day.

north of the equator (4°–4.5°C) and slightly weaker cooling south of the equator (~2.5°C). Reduced easterlies over the Atlantic, caused by increased JJA African monsoon winds, cause the thermocline to shoal in the western Atlantic by ~20 m. The speed of the simulated equatorial undercurrent is therefore weaker, dropping from 70 cm s^{-1} for the present day to 40 cm s^{-1} in the LGM.

The extent of annual mean sea ice in the simulations (Figure 20) indicate, in general, an expansion in the Northern Hemisphere and a retreat in the Southern Hemisphere. Despite the fact that the areal extent of sea ice is well simulated for the present day (compare Figures 20a and 20b to *Untersteiner* [1984], for example), the extent of sea ice in the LGM simulation is smaller than in paleoreconstructions, particularly in the Southern Hemisphere, where there is significantly less ice

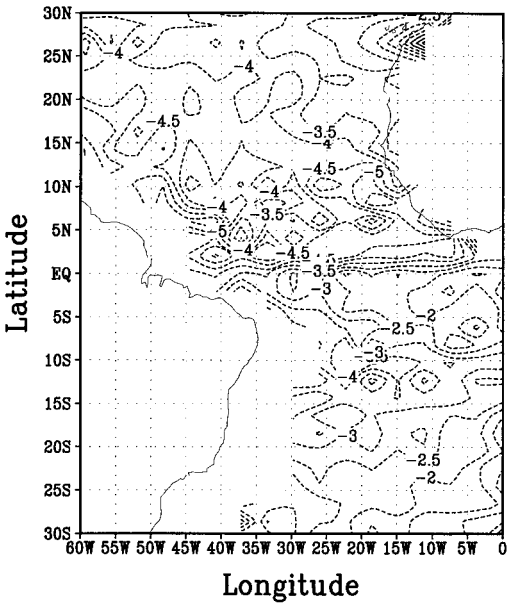

Figure 19. Difference in annual mean SST in the tropical Atlantic Ocean (LGM minus present day; contour interval 0.5°C).

than at present (Figure 20e). A lack of sea ice in the Southern Hemisphere was also noted in the LGM simulation of *Manabe and Broccoli* [1985a] who employed the same atmospheric model (in a slightly different configuration) coupled to a mixed-layer ocean model. In the Northern Hemisphere, simulated LGM sea ice is in better agreement with CLIMAP reconstructions, although the maximum extent appears to be somewhat underestimated. In particular, the annual mean ice margin advances beyond Iceland to the east but not in the Denmark Strait; additionally, the southern tip of Greenland is ice free in the simulation, whereas it is not in the CLIMAP reconstructions. However, analyses of dinocyst assemblages in the North Atlantic indicate that the CLIMAP reconstructions may have underestimated LGM summertime temperatures and thereby overestimated sea ice amounts [*de Vernal et al*., 1994; A. de Vernal et al., Sea surface conditions in middle to high latitudes of North Atlantic during the last glacial maximum (LGM): The cold paradigm revisited, submitted to *Canadian Journal of Earth Sciences*, 1999.)

4. Discussion and Conclusions

This LGM simulation reproduces many of the main features of previous atmosphere-only or atmosphere-mixed-layer ocean simulations. Anticyclonic circulations about the ice sheets, intensification of Atlantic storm track winds, and ~10°–15°C mean annual cooling of Northern Hemisphere continents are all fairly robust traits of ice age simulations, even though the simulations may be performed by different models [e.g., *Manabe and Broccoli*, 1985a; *Rind and Peteet*, 1985; *Kutzbach and Guetter*, 1986; *Hall et al*., 1996].

The unique aspect of this simulation is the inclusion of coupled atmosphere-ocean dynamics into the calculations. As the spatial resolution of the ocean model, which is maximized under computational constraints, precludes centennial or millenial integrations, one can consider this simulation as a GCM with a "mixed layer plus upper ocean dynamics" model. A longer integration time would, of course, allow for deep baroclinic ocean currents to form and for the possibility of climate variability on longer timescales than decadal.

The effect of glacial ice sheets on the simulated atmosphere-ocean climate is twofold. First, they induce substantially colder temperatures both locally and downwind. Second, they induce changes in the strength and direction of the tropospheric winds. Both of these are important factors in determining the LGM ocean circulation: lower temperature downwind of the ice sheets increases the sensible heat flux out of the ocean, and changes in the winds alter the spatial patterns of both the wind stress curl and the buoyancy forcing. Stronger and colder LGM winds over the North Atlantic produce a 9°C SST cooling and a more zonally oriented Gulf Stream.

A stronger baroclinic zone over the North Atlantic (compare Figures 3 and 6) would increase the frequency of baroclinic wave development since the growth rate of these waves increases with baroclinicity [e.g., *Bush and Peltier*, 1994]. An increase in eddy activity in LGM storm tracks has been noted previously by *Hall et al*. [1996].

Increased equatorward transport of easterly momentum via eddy momentum fluxes during the later stages of baroclinic wave life cycles increases the strength of the Northern Hemisphere Hadley cell by 20% in the LGM simulation (not shown). Additionally, increased equatorward transport of easterly momentum implies more relative westerly angular momentum in the midlatitude belts and less in the tropics. The relative angular momentum in the simulations is calculated as $M = \int uR \cos(\phi)\, dm$ in the latitude belts between 90°S–20°S, 20°S–20°N, and 20°N–90°N as well as for the Northern and Southern Hemispheres (here M is the relative angular momentum, u is the zonal wind speed, R is the Earth's radius, ϕ is latitude, and dm is an element of mass). The results for the two simulations are summarized in Table 2. In an annual mean the LGM equatorial atmosphere has a ~56% increase in relative easterly angular momentum between 20°S and 20°N; climatologically, this is evident in the increased easterly Pacific trade winds (compare Figures 8 and 11). The majority of this increase occurs in the Northern Hemisphere winter (DJF), which is the season of maximum baroclinic wave development. In the Southern Hemisphere midlatitudes the LGM simulation produces consistently smaller values of relative westerly angular momentum; these are sufficient to bring the global, annual mean total to 2.8×10^{25} kg m^2 s^{-1} below that of the present day. (This difference would translate into a 5×10^{-4} s shortening of the glacial length of day (LOD) due to relative momentum changes in the atmosphere, a value that is comparable to the amplitude of modern LOD diurnal fluctuations [e.g., *Peixoto and Oort*, 1992].)

Stronger easterly trades over the Pacific imply an intensification of the mean South Equatorial Current (SEC), an increase in the tilt of the mean equatorial thermocline, and an increase in strength of the mean Equatorial Undercurrent. A stronger SEC increases the westward advection of cold SST, increasing the extent of the cold tongue and cooling the western Pacific by ~13 W m^{-2}. Additionally, stronger Ekman divergence along the equator increases cooling by vertical advection by nearly 6 W m^{-2}. Colder SST in the western Pacific decreases the amount of convection in the area, increasing the incoming shortwave radiation enough to balance the advective cooling in the time-mean thermodynamic equation (for further details, see *Bush and Philander* [1998]).

A simplified picture that emerges from the simulation is as

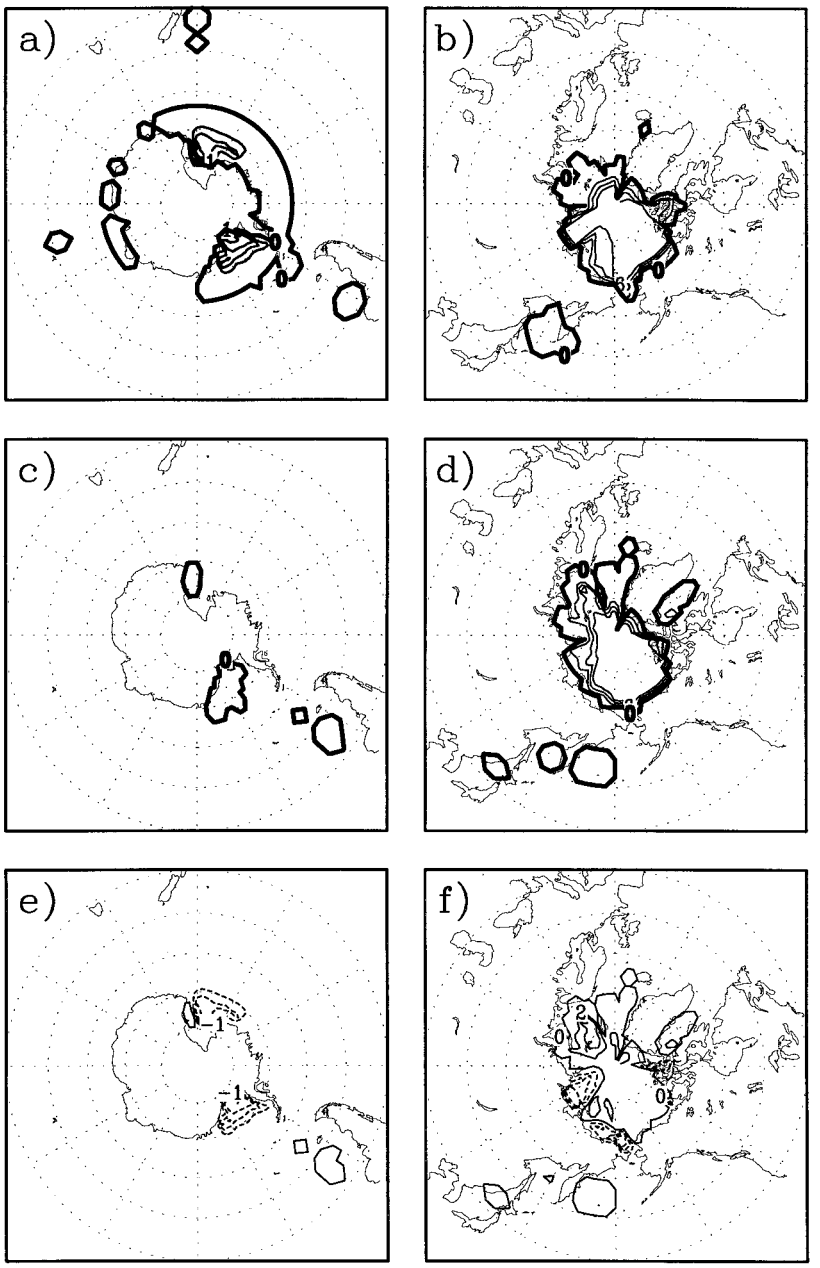

Figure 20. Annual mean sea ice amount (in meters, contour interval 1 m) and extent (as indicated by the thick black line) for the (a) Southern Hemisphere for present day, (b) Northern Hemisphere for present day, (c) Southern Hemisphere for LGM, (d) Northern Hemisphere for LGM, (e) Southern Hemisphere and (f) Northern Hemisphere difference (LGM minus present day).

Table 2. Relative Angular Momentum in the Two Simulations

	Annual Mean	DJF	JJA
	16.8 (14)	18 (14)	15.5 (11.1)
90°S–20°S	10.8 (9)	9 (6.6)	12.6 (11)
20°S–20°N	−0.96 (−1.5)	−0.9 (−2.6)	−1.1 (−1.2)
20°N–90°N	7 (6.1)	9.9 (10)	4 (1.3)
0°N–90°N	6.4 (5.3)	9.6 (8.8)	3.2 (0.32)
0°S–90°S	10.4 (8.4)	8.5 (5.2)	12.3 (11)

Momentum, $M = \int uR \cos(\phi)\, dm$, is in units of 10^{25} kg m^2 s^{-1}. Values in parentheses are from the LGM simulation. DJF is December-January-February; JJA is June-July-August.

follows. Stronger Northern Hemisphere baroclinicity induces more frequent baroclinic waves. These waves increase the strength of the mean meridional circulation and the equatorward transport of easterly momentum. Easterly relative angular momentum increases in the tropics, particularly over the Pacific basin. Consequently, in the Pacific Ocean the wind-driven SEC is stronger and more equatorial upwelling is produced; the tilt of the thermocline increases. Convection decreases over the western Pacific, and the cloud amount is reduced. Increased solar radiation then balances the cold advection until a steady state is achieved. The westward shift in convection induces a baroclinic Rossby wave response in the

tropical atmosphere which strengthens even further the tropical easterlies. Colder tropical SST and reduced evaporation decrease the amount of water vapor in the atmosphere by 10% in a global mean, with the greatest reduction (up to 20%) occurring in the tropics. As water vapor is a greenhouse gas, this also feeds back on the global mean temperature to further cool the planet.

Tropical SST cooling of 4°–6°C and reduced amounts of atmospheric water vapor combine to cool the tropical atmosphere to a degree not previously simulated. SST changes in the tropical Pacific Ocean have the largest climatic impact of any ocean basin, given the large surface area of the equatorial Pacific. Closer agreement between simulated LGM temperature depressions over tropical continents and recent proxy data is encouraging and suggests that dynamical interactions between the atmosphere and the oceans play an important role in regulating lowland continental temperatures. It has been shown by *Rind and Peteet* [1985] that, in an atmospheric GCM, SSTs that are 2°C colder than the CLIMAP reconstructions produce continental temperatures that are in much better agreement with the continental proxy data. Dynamical atmosphere-ocean interactions therefore appear to be necessary in order to produce the tropical SSTs which then cool the atmosphere and reduce atmospheric water vapor such that a 6°–7°C cooling over tropical landmasses is simulated.

Cooling of the Southern Hemisphere landmasses (see Figure 3) is much greater than that produced with a mixed-layer ocean model [*Manabe and Broccoli*, 1985a] and is a consequence of the enhanced tropical cooling. Over the high southern latitude oceans, however, there is little simulated temperature change or, in the regions of reduced sea ice, an actual temperature increase. The baroclinic structure of the southern midlatitudes is therefore weakened (see Figure 4), and the strength of the geostrophic winds, the frequency of eddy activity, and the strength of the Southern Hemisphere Hadley cell are all reduced. Reductions in snowfall along the Antarctic coast, particularly in the Weddell and Ross Seas, decrease local sea ice accumulation. The reduction in trade wind speeds appears to be inconsistent with the 30–50% increase in the South Pacific trades as inferred from upwelling variations along the Peru Current [*Molina-Cruz*, 1977]. Further analysis is required in order to explain this discrepancy.

Simulated changes in the annual mean thermocline depth at the LGM imply that interannual and decadal variability would be different than today because the equatorward displacement of the oceanic subduction zones implies a shorter distance that subducted water would have to travel to reach the equator. This, in turn, would shorten the period of LGM "decadal" climate fluctuations since the period of this variability is determined by the time taken for water to flow from the subduction zone to the equator [*Gu and Philander*, 1997]. Such intriguing questions remain the subject of future research as we learn more about decadal and centennial variability in our present climate. It remains therefore only to list some of the model results that we perceive to be worth further investigation.

1. The decrease in areal extent of sea ice around Antarctica deserves to be examined in more detail, given the fact that present-day amounts are well simulated. It needs to be determined whether this is a model bias under glacial forcing or whether it is simply part of a longer-timescale fluctuation. The role of reduced atmospheric water vapor on the hydrological cycle in the Southern Ocean needs to be examined.

2. The role of the ocean in determining interior continental temperatures needs to be investigated further. Whether water vapor feedback or temperature advection is primarily responsible needs to be assessed through a diagnostic study.

3. The impact of longer-timescale ocean dynamics needs to be explored through a longer integration, preferably without loss of spatial resolution in order to keep the interior dynamics as inviscid as possible. A direct comparison to the results of *Weaver et al*. [1998] is presently underway in order to clarify precisely the roles of the wind-driven and deep ocean circulations in determining SST (and hence the climate).

Acknowledgments. ABGB acknowledges support from the Natural Sciences and Engineering Research Council of Canada (OGP0194151 and the Climate System History and Dynamics Project). SGHP acknowledges support from the National Oceanic and Atmospheric Administration (NA86GP0338 and NA56GP0226). Both authors thank Rick Fairbanks and an anonymous reviewer for helpful comments on a previous version of the manuscript.

References

Andreasen, D., and A. C. Ravelo, Tropical Pacific Ocean thermocline depth reconstructions for the Last Glacial, *Paleoceanography*, *12*, 395–414, 1997.

Berger, A., Orbital variations and insolation database, IGBP PAGES, World Data Cent. A for Paleoclimatology, *Data Contrib*., *Ser. 92-007*, Natl. Geophys. Data Cent., Boulder, Colo., 1992.

Broccoli, A. J., and S. Manabe, The influence of continental ice, atmospheric CO_2, and land albedo on the climate of the last glacial maximum, *Clim. Dyn*., *1*, 87–99, 1987.

Broccoli, A. J., and E. P. Marciniak, Comparing simulated glacial climate and paleodata: A reexamination, *Paleoceanography*, *11*, 3–14, 1996.

Broecker, W., Oxygen isotope constraints on surface ocean temperatures, *Quat. Res*., *26*, 121–134, 1986.

Bryan, K., A numerical method for the study of the circulation of the world ocean, *J. Comput. Phys*., *3*, 347–376, 1969.

Bush, A. B. G., and W. R. Peltier, Tropopause folds and synoptic-scale baroclinic wave life cycles, *J. Atmos. Sci*., *51*, 1581–1604, 1994.

Bush, A. B. G., and S. G. H. Philander, The ocean-atmosphere interactions in tropical cooling during the Last Glacial Maximum, *Science*, *279*, 1341–1344, 1998.

Climate: Long-Range Investigation, Mapping, and Prediction (CLIMAP) Project Members, Seasonal reconstructions of the Earth's surface at the last glacial maximum, *Map and Chart Ser. MC-36*, Geol. Soc. of Am., Boulder, Colo., 1981.

Colinvaux, P. A., P. E. De Oliveira, J. E. Moreno, M. C. Miller, and M. B. Bush, A long pollen record from lowland Amazonia: Forest and cooling in glacial times, *Science*, *274*, 85–88, 1996.

de Vernal, A., J.-L. Turon, and J. Guiot, Dinoflagellate cyst distribution in high latitude environments and quantitative reconstruction of sea-surface temperature, salinity and seasonality, *Can. J. Earth Sci*., *31*, 48–62, 1994.

Fairbanks, R. G., A 17,000-year glacio-eustatic sea level record: Influence of glacial melting rates on Younger Dryas event and deep-ocean circulation, *Nature*, *342*, 637–642, 1989.

Fanning, A. F., and A. J. Weaver, An atmospheric energy-moisture balance model: Climatology, interpentadal climate change, and coupling to an ocean general circulation model, *J. Geophys. Res*., *101*, 15,111–15,128, 1996.

Flenley, J. R., The Quaternary vegetational history of the equatorial mountains, *Prog. Phys. Geogr*., *3*, 488–509, 1979.

Gates, W. L., Modeling the ice-age climate, *Science*, *191*, 1138–1144, 1976a.

Gates, W. L., The numerical simulation of ice-age climate with a global general circulation model, *J. Atmos. Sci*., *33*, 1844–1873, 1976b.

Gordon, C. T., and W. Stern, A description of the GFDL global spectral model, *Mon. Weather Rev*., *110*, 625–644, 1982.

Gu, D., and S. G. H. Philander, Interdecadal climate fluctuations that depend on exchanges between the tropics and extratropics, *Science*, *275*, 805–807, 1997.

Guilderson, T. P., R. G. Fairbanks, and J. L. Rubenstone, Tropical

temperature variations since 20,000 years ago: Modulating interhemispheric climate change, *Science*, *263*, 663–665, 1994.
Hall, N. M. J., P. J. Valdes, and B. Dong, The maintenance of the last great ice sheets: A UGAMP GCM study, *J. Clim*., *9*, 1004–1019, 1996.
Hyde, W. T., T. J. Crowley, K.-Y. Kim, and G. R. North, Comparison of GCM and energy balance model simulations of seasonal temperature changes over the past 18,000 years, *J. Clim*., *2*, 864–887, 1989.
Jolly, D., and A. Haxeltine, Effect of low glacial atmospheric CO_2 on tropical African montane vegetation, *Science*, *276*, 786–788, 1997.
Kutzbach, J. E., and P. J. Guetter, The influence of changing orbital parameters and surface boundary conditions on climate simulations for the past 18,000 years, *J. Atmos. Sci*., *43*, 1726–1759, 1986.
Kutzbach, J. E., and H. E. Wright, Simulations of the climate of 18,000 yr BP: Results for the North American/north Atlantic/European sector and comparison with the geologic record, *Quat. Sci. Rev*., *4*, 147–187, 1985.
Levitus, S., Climatological atlas of the world ocean, *NOAA Prof. Pap. 13*, 173 pp., U.S. Govt. Print. Office, Washington, D. C., 1982.
Lyle, M. W., F. G. Prahl, and M. A. Sparrow, Upwelling and productivity changes inferred from a temperature record in the central equatorial Pacific, *Nature*, *355*, 812–815, 1992.
Manabe, S., and A. J. Broccoli, The influence of continental ice sheets on the climate of an ice age, *J. Geophys. Res*., *90*, 2167–2190, 1985a.
Manabe, S., and A. J. Broccoli, A comparison of climate model sensitivity with data from the last glacial maximum, *J. Atmos. Sci*., *42*, 2643–2651, 1985b.
Manabe, S., and D. G. Hahn, Simulation of the tropical climate of an ice age, *J. Geophys. Res*., *82*, 3889–3911, 1977.
Manabe, S., and R. J. Stouffer, Sensitivity of a global climate model to an increase of concentration in the atmosphere, *J. Geophys. Res*., *85*, 5529–5554, 1980.
Molina-Cruz, A., The relation of the southern trade winds to upwelling processes during the last 75,000 years, *Quat. Res*., *8*, 324–338, 1977.
Navarra, A., W. F. Stern, and K. Miyakoda, Reduction of the Gibbs oscillation in spectral model simulations, *J. Clim*., *7*, 1169–1183, 1994.
Pacanowski, R. C., and S. G. H. Philander, Parameterization of vertical mixing in numerical models of tropical oceans, *J. Phys. Oceanogr*., *11*, 1443–1451, 1981.
Pacanowski, R. C., K. Dixon, and A. Rosati, The GFDL Modular Ocean Model user guide, *GFDL Ocean Group Tech. Rep. 2*, Geophys. Fluid Dyn. Lab., Princeton, N. J., 1991.
Parkin, D. W., and N. J. Shackleton, Trade wind and temperature correlations down a deep-sea core off the Saharan coast, *Nature*, *245*, 455–457, 1973.
Pedersen, T. F., Increased productivity in the eastern equatorial Pacific during the last glacial maximum (19,000 to 14,000 yr B.P.), *Geology*, *11*, 16–19, 1983.
Pedlosky, J., *Ocean Circulation Theory*, 453 pp., Springer-Verlag, New York, 1996.
Peixoto, J. P., and A. H. Oort, *Physics of Climate*, 520 pp., Am. Inst. of Phys., College Park, Md., 1992.
Peltier, W. R., Ice age paleotopography, *Science*, *265*, 195–201, 1994.
Peterson, G. M., T. Webb III, J. E. Kutzbach, T. Van der Hammen, T. A. Wijmstra, and F. A. Street, The continental record of environmental conditions at 18,000 yr B.P.: An initial evaluation, *Quat. Res*., *12*, 47–82, 1979.
Philander, S. G. H., D. Gu, D. Halpern, G. Lambert, N.-C. Lau, T. Li, and R. C. Pacanowski, Why the ITCZ is mostly north of the equator, *J. Clim*., *9*, 2958–2972, 1995.
Ravelo, A. C., R. G. Fairbanks, and S. G. H. Philander, Reconstructing tropical Atlantic hydrography using planktonic foraminifera and an ocean model, *Paleoceanography*, *5*, 409–431, 1990.
Rind, D., and D. Peteet, Terrestrial conditions at the last glacial maximum and CLIMAP sea-surface temperature estimates: Are they consistent?, *Quat. Res*., *24*, 1–22, 1985.
Salgado-Labouriau, M. L., V. Casseti, K. R. Ferraz-Vicentini, L. Martin, F. Soubiès, K. Suguio, and B. Turcq, Late Quaternary vegetational and climatic changes in cerrado and palm swamp from central Brazil, *Palaeogeogr. Palaeoclimatol. Palaeoecol*., *128*, 215–226, 1997.
Sarnthein, M., G. Tetzlaff, B. Koopman, K. Wolter, and U. Pflaumann, Glacial and interglacial wind regimes over the eastern subtropical Atlantic and north-west Africa, *Nature*, *293*, 193–196, 1981.
Schrag, D. P., G. Hampt, and D. W. Murray, Pore fluid constraints on the temperature and oxygen isotopic composition of the glacial ocean, *Science*, *272*, 1930–1932, 1996.
Street-Perrott, F. A., and S. P. Harrison, Lake levels and climate reconstruction, in *Paleoclimate Analysis and Modeling*, edited by A. D. Hecht, pp. 291–340, John Wiley, New York, 1985.
Stute, M., M. Forster, H. Frischkorn, A. Serejo, J. F. Clark, P. Schlosser, W. S. Broecker, and G. Bonani, Cooling of Tropical Brazil (5°C) during the last glacial maximum, *Science*, *269*, 379–383, 1995.
Thompson, L. G., E. Mosley-Thompson, M. E. Davis, P.-N. Lin, K. A. Henderson, J. Cole-Dai, J. F. Bolzan, and K.-B. Liu, Late glacial stage and Holocene tropical ice core records from Huascarán, Peru, *Science*, *269*, 46–50, 1995.
Untersteiner, N., The cryosphere, in *The Global Climate*, edited by J. T. Houghton, pp. 121–140, Cambridge Univ. Press, New York, 1984.
Weaver, A. J., M. Eby, A. F. Fanning, and E. C. Wiebe, Simulated influence of CO_2, orbital forcing and ice sheets on the climate of the last glacial maximum, *Nature*, *394*, 847–853, 1998.
Webb, R. S., D. H. Rind, S. J. Lehman, R. J. Healy, and D. Sigman, Influence of ocean heat transport on the climate of the Last Glacial Maximum, *Nature*, *385*, 695–699, 1997.
Wetherald, R. W., and S. Manabe, Cloud feedback processes in a general circulation model, *J. Atmos. Sci*., *45*, 1397–1415, 1988.
Whitlock, C., and P. J. Bartlein, Vegetation and climate change in northwest America during the past 125 kyr, *Nature*, *388*, 57–60, 1997.

A. B. G. Bush, Department of Earth and Atmospheric Sciences, University of Alberta, 126 Earth Sciences Building, Edmonton, Alberta, Canada T6G 2E3. (andrew.bush@ualberta.ca)

S. G. H. Philander, Program in Atmospheric and Oceanic Sciences, Princeton University, P.O. Box CN710, Sayre Hall, Princeton, NJ 08544-0710. (gphlder@splash.princeton.edu)

(Received October 5, 1998; revised May 12, 1999;
accepted May 19, 1999.)